Assessing the coupling between the SSG-LRR Reynolds stress model and the $\gamma - Re_\theta$ transition model

Pedro Movilha Nogueira da Silva

pedromovilhasilva@tecnico.ulisboa.pt

Instituto Superior Técnico, Universidade de Lisboa, Portugal

August 2021

Abstract

The use of new methods to simulate transitional flows is gaining increasing importance in the world of aerodynamics. In the middle Reynolds number range ($10^5 - 10^7$), with applications ranging from the flow around a drone to the study of models to be used in a wind-tunnel, the use of RANS approach with turbulence models coupled with a method for predicting transition appears as an accurate and cheaper alternative to other methods, such as DNS or LES. In the RANS approach, one of the most precise methods for modelling turbulence is the RSMs. RSMs present the advantage of not being isotropic and are viewed as being the accurate alternative for time-averaged RANS simulations when compared to EVMs. Coupling this with a reliable transition-prediction method is, therefore, something that must be tried out in order to verify that the results obtained are satisfactory and accurate when compared to other turbulence predicting methods, and with experimental data.

The focus of this work is then to apply the RANS equations for modelling and capture the mean properties of a transitional flow. These equations are closed with the SSG-LRR-ω, coupled with the $\gamma - Re_\theta$ transition model. Several test-cases are studied: a flat plate, an airfoil, and a 6:1 prolate spheroid. It was found that this coupling presented a greater grid dependance than the $k - \omega$ SST + $\gamma - Re_\theta$ coupling, and displayed more difficulties in achieving iterative convergence, specially in regions with flow separation. The inlet turbulence boundary conditions tuned to be used with the $k - \omega$ SST + $\gamma - Re_\theta$ were found to be not the most suitable for the SSG-LRR-ω + $\gamma - Re_\theta$, with this latter coupling being less sensitive to changes in the inlet turbulence conditions than the first one. In all the simulations performed, the SSG-LRR-ω + $\gamma - Re_\theta$ took longer to react to the inlet conditions, and presented transition downstream of the $k - \omega$ SST + $\gamma - Re_\theta$.

Keywords: RANS, SSG-LRR-ω, $\gamma - Re_\theta$, transitional flow

---

1. Introduction

The constant pursuit of new ways of simulating increasingly complex transitional flows motivates inumerous studies and research in the aerodynamics field [30–32]. For the past few years, new tools have been developed, with the purpose of increasing the simulation's modelling accuracy, without a significant rise in the computational costs. For cases of transitional flows, where a significant part of the flow is laminar, the use of the Reynolds averaged Navier Stokes (RANS) mathematical approach with a Reynolds stress model (RSM) to model turbulence, coupled with a reliable transition prediction method is emerging as an alternative to other numerical methods such as the direct numerical simulation (DNS), large eddy simulation (LES), or the e^N method. RSMs present the advantage of being able to deal with turbulence anisotropy and are often regarded as being a more accurate alternative for time-averaged RANS simulations, when compared to eddy viscosity based models (EVMs). Combining RSMs with transition models can be advantageous in geometries with strong curvature, with rotational flows [17], where other models as the $k - \omega$ SST model [26] might be less reliable. The focus of this work draws upon assessing the coupling between the SSG-LRR-ω Reynolds stress model [9] and the $\gamma - Re_\theta$ transition model [20].

There are two main objectives of this research:

1. Evaluate the numerical robustness of the SSG-LRR-ω + γ-Re_θ combination, i.e. check the ability to reduce the residuals to negligible levels;

2. Evaluate the influence of inlet turbulence boundary conditions on the location of transition predicted with the SSG-LRR-ω+γ-Re_θ combination and compare it with the results obtained with the $k - \omega$ SST+γ-Re_θ combination;

To fullfill these objectives, three different test cases were selected, each one having different goals: a 2D study of a flow over a flat plate, which allows the use of an inlet boundary relatively close to the leading edge; a 2D study of a flow around the NFL1-0416 airfoil that exhibits separation induced transition as well as natural transition; a 3D study of a flow around a prolate spheroid to include a three-dimensional geometry.

2. Transitional Flows Overview

Simulating flows around bodies with complex geometries is fundamental in the design process of engineering projects. To study transitional flows, such as the flow around a drone, or the study of wind tunnel models, methods known for their superior accuracy such as the direct numerical simulation (DNS) can be a possibility. However, it is currently suitable to simulate problems only at relatively low Reynolds numbers. Other methods, such as the large eddy simulation (LES) appear as simplification of the DNS approach, but has a poor behaviour in near-wall

conditions. Other tools increasingly used nowadays to simulate transitional flows near walls draw upon some simplification of the Navier-Stokes equations such as in the case of the Reynolds Averaged Navier-Stokes (RANS) equations. This mathematical method averages the continuity and momentum equations, and all the dependant variables, requiring a turbulence model to perform the so-called "closure of the problem" [14].

2.1. **Turbulence Models**
Some turbulence models, the eddy viscosity based models (EVMs), such as the $k - \omega$ SST, obtain the Reynolds stresses through a previously established assumption, such as the Boussinesq hypothesis [7]. They are numerically stable, and versatile. However, they assume the turbulence to be isotropic, which make them poor models for flows with strong curvature and rotation.

On the other hand, the Reynolds stress models, such as the SSG-LRR-ω assume themselves as an alternative to EVMs. They can deal with the anisotropy of turbulence, due to the redistribution of the Reynolds stresses coming from the pressure-strain correlation. This makes RSMs more accurate than EVMs in predicting flows with normal Reynolds stress anisotropy [18] and flows with large amounts of rotation, such as the free vortices created in the tip of a plane's wing [8]. It is also indicated for flows with strong curvature [17], or with large instability regions [15] and strong adverse pressure gradients [30].

2.2. **Transition Model**
Except for the DNS and LES, that can be used for transitional flows [6], but presents the disadvantages mentioned before, the previously discussed models are not suitable to model transition on their own [13], since they usually predict transition sooner than what is verified in the real flow. Therefore, in order that ensure that transition phenomena occuring in the flow are captured with the maximum accuracy possible, one should complement the turbulence model with a suitable method for predicting and modelling transition.

Several transition prediction methods and models have been developed, and it is possible to enumerate some of them, such as the linear stability theory based e^N method, empirical non-local correlation based methods, or local transport equation based transition models, such as the $\gamma - Re_\theta$ model. The e^N method is a commonly used non-local method [35] that needs access to integral parameters of the flow. In RANS applications, where there is usually a decomposition of the domain by several computational cores, it is hard to implement this non-local method: one processing core could need information stored in another one, requiring an additional computational effort, since this passage of information is usually time-consuming.

The e^N method also presents some more downsides, since it is limited to some transition mechanisms, and only provides the location of the transition point, meaning it "activates" the turbulence model downstream of that point, creating a discontinuity in the domain [35]. Empirical non-local correlation based methods [28] are not used much anymore nowadays, having been replaced by other more reliable methods.

Local transport equation based transition models such as the γ model [29] or the $\gamma - Re_\theta$ model [20] are frequently and easily coupled with RANS applications [22]. Being local models, they only require information available in the cell, and do not make use of integral parameters. Therefore, the domain partition by several computational cores that are commonly used with RANS does not hinder the model to obtain the information it requires.

In this work, the $\gamma - Re_\theta$ model was the chosen transition model to be coupled with the SSG-LRR-ω model, since this work follows the work reported in [22], within the scope of the MARIN-IST cooperation.

2.3. ReFRESCO Software
The 2.6 version of the ReFRESCO software was used in all the computations performed in the present work. As defined in the official website [4], "ReFRESCO is a viscous-flow CFD code that solves multiphase (unsteady) incompressible flows using the Navier-Stokes equations, complemented with turbulence models (...) Various turbulence models, from RANS models to high fidelity hybrid and scale resolving models, complemented with transition models are available. The equations are discretised using a finite-volume approach discretization of the RANS and turbulence quantities transport equations, with cell-centered collocated variables, in strong conservation form. (...)" ReFRESCO enables a segregated or coupled solution of the continuity and momentum equations. On the other hand, the solution of the k and ω transport equations is always segregated. Therefore, all the simulations presented in this work were performed with the segregated approach. There was a crossflow transition prediciton method available, but it was decided not to include it in the model. In all the simulations made with ReFRESCO, the fluid is assumed to be Newtonian, single-phase and incompressible. The dynamic molecular viscosity μ is also constant in a simulation.

3. **Mathematical Model**
To describe flows of viscous, incompressible fluids, one can resort to mass conservation and momentum balance, which can be expressed in a Cartesian coordinate system as:

$$\frac{\partial \tilde{V}_i}{\partial x_i} = 0.$$
$$\frac{\partial \left(\rho \tilde{V}_i \right)}{\partial t} + \frac{\partial \rho \tilde{V}_i \tilde{V}_j}{\partial x_j} = -\frac{\partial \tilde{P}}{\partial x_i} + \frac{\tau_{ij}}{\partial x_j}. \tag{1}$$

Being $\tilde{V}_i$ the instantaneous Cartesian velocity components, ρ the fluid density, $\tilde{P}$ is the relative pressure (with the reference pressure being the hydrostatic pressure). The subscripts i and j are computational indexes representing consecutive, non-equal cartesian coordinates x, y, z and τ_{ij} stands for the components of the stress tensor, which for a Newtonian fluid is given by:

$$\tau_{ij} = \mu \left(\frac{\partial \tilde{V}_i}{\partial x_j} + \frac{\partial \tilde{V}_j}{\partial x_i} \right). \tag{2}$$

Being the three test-cases evaluated wall bounded transitional flows, the RANS approach can be used, meaning that all instantaneous flow variables $\tilde{\Phi}$ are decomposed in a mean value Φ and a fluctuation ϕ (turbulence). To discover a variable $\tilde{\Phi}$, different type of averaging can be used, depending on the physics of the flow. For the flows analysed in this work, where the mean flow is statistically steady, time-averaging can be applied, being defined by equation 3:

$$\Phi(x_i) = \lim_{T \to \infty} \frac{1}{T} \int_0^T \tilde{\Phi}(x_i, t) dt. \tag{3}$$

Applying equation 3 to the variables in the continuity and momentum equations 1, one obtain the RANS equations, defined by:

$$\frac{\partial V_i}{\partial x_i} = 0,$$
$$\frac{\partial \rho V_i V_j}{\partial x_j} = -\frac{\partial P}{\partial x_i} + \frac{\partial}{\partial x_j} \left(\mu \left(\frac{\partial V_i}{\partial x_j} + \frac{\partial V_j}{\partial x_i} \right) - \rho \overline{v_i v_j} \right). \tag{4}$$

This leads to a statistically steady flow. However, it also generates the Reynolds stress tensor $-\rho\overline{v_i v_j}$ patent in the momentum equation, where the overbar represents the average value.

The notation used in this work for the Reynolds stresses is ρR_{ij}, that is equivalent to $-\rho\overline{v_i v_j}$. This additional term requires closure, implying the formulation of an extra equation, i.e. writing this term as a function of known variables of the flow [12]. This is achieved by using a turbulence model, that will prescribe the values of the Reynolds stresses, through modeling approximations, allowing the computational solving of these equations. To prescribe the values for the Reynolds stresses, turbulence models can follow different approaches.

3.1. EVMs

Some turbulence models, called eddy viscosity based models (EVM), make use of a "mathemathical concept" called **eddy viscosity** μ_t, first described by Joseph Boussinesq in [7]. These models involve a previously established assumption, that relates the eddy viscosity with the Reynolds stresses, such as the Boussinesq hypothesis [7] The way eddy viscosity is calculated nowadays depends on the formulation that each model uses, but the fundamental goal is to define it using known flow variables.

3.1.1 $k-\omega$ SST model

The $k-\omega$ SST turbulence model is a two-equation eddy viscosity model, presented in [26]. The formulation used in this work follows the expressions that can be found in [3]. It features two transport equations, for the turbulent kinetic energy k and the specific turbulent dissipation rate ω.

The two-equation model, for incompressible flow can be written, in conservation form, for steady flows as in equations 5 and 6:

$$\frac{\rho\partial\left(V_j k\right)}{\partial x_j}=P_k-D_k+\frac{\partial}{\partial x_j}\left[(\mu+\sigma_k\mu_t)\frac{\partial k}{\partial x_j}\right], \qquad (5)$$

$$\frac{\rho\partial\left(V_j\omega\right)}{\partial x_j}=P_\omega-D_\omega+\frac{\partial}{\partial x_j}\left[(\mu+\sigma_\omega\mu_t)\frac{\partial\omega}{\partial x_j}\right]+2(1-F_1)\frac{\rho\sigma_{\omega2}}{\omega}\frac{\partial k}{\partial x_j}\frac{\partial\omega}{\partial x_j}. \qquad (6)$$

3.1.2 $k-\sqrt{k}L$ model

The $k-\sqrt{k}L$ model is a linear eddy viscosity model, that features two transport equations, one for $\phi=\sqrt{k}L$, with L being the turbulent length scale, and another for k. This model is also used in ReFRESCO, and provides extra data for comparison. The formulation used in this work follows the expressions that can be found in [27].

The two-equation model, written in conservation form, for steady, incompressible flow, is given by the following:

$$\frac{\rho\partial\left(V_j k\right)}{\partial x_j}=P_k-D_k+\frac{\partial}{\partial x_j}\left[(\mu+\sigma_k\mu_t)\frac{\partial k}{\partial x_j}\right]. \qquad (7)$$

$$\frac{\rho\partial\left(V_j\phi\right)}{\partial x_j}=C_{\phi1}\frac{\phi}{k}P-C_{\phi2}\rho k^{3/2}-6\mu\frac{\phi}{d^2}f_\phi+\frac{\partial}{\partial x_j}\left[(\mu+\sigma_\phi\mu_t)\frac{\partial\phi}{\partial x_j}\right]. \qquad (8)$$

3.2. RSMs

There are other turbulence models, the Reynolds stress models (RSM), that directly compute the Reynolds stresses, requiring additional equations to do so.

3.2.1 RSM - SSG-LRR-ω model

The SSG-LRR-ω model is a blend between the Speziale-Sarkar-Gatski model (SSG) [34] in the far field and the Launder-Reece-Rodi (LRR) model [21] near walls, combined with Menter's baseline ω-equation for the length scale [9]. The formulation used in this work follow the expressions that can be found in [5].

The SSG-LRR-ω is a full second-moment Reynolds stress model [10, 15, 16], meaning it computes each of the 6 Reynolds stresses directly, with each Reynolds stress having its own transport equation. There is also a seventh transport equation for the ω variable. The six Reynolds stresses, for steady flows, are given by equation 9:

$$\frac{\rho\partial(V_k R_{ij})}{\partial x_k}=\rho D_{ij}+\rho P_{ij}+\rho\Pi_{ij}-\rho\epsilon_{ij}+\rho M_{ij}. \qquad (9)$$

The equation for the specific rate of dissipation ω for steady flows is given by:

$$\frac{\rho\partial(V_k\omega)}{\partial x_k}=P_\omega-D_\omega+\frac{\partial}{\partial x_k}\left[\left(\mu+\sigma_\omega\frac{\rho k}{\omega}\right)\frac{\partial\omega}{\partial x_k}\right]+\sigma_d\frac{\rho}{\omega}max\left(\frac{\partial k}{\partial x_j}\frac{\partial\omega}{\partial x_j},0\right). \qquad (10)$$

3.3. Transition Model

3.3.1 $\gamma-Re_\theta$

The $\gamma-Re_\theta$ transition model is a two-equation model used to model transitional flows where a significant portion of the boundary layer is laminar. It solves transport equations for the intermittency factor, γ, represented in equation 11 which indicates the state of the flow, and the transition momentum thickness Reynolds number, $Re_{\theta t}$, represented in equations 12. The formulation used in this work for this model follows the equation found in [2].

$$\frac{\rho\partial(\gamma)}{\partial t}+\frac{\rho\partial\left(V_j\gamma\right)}{\partial x_j}=P_\gamma-D_\gamma+\frac{\partial}{\partial x_j}\left[\left(\mu+\frac{\mu_t}{\sigma_f}\right)\frac{\partial\gamma}{\partial x_j}\right]. \qquad (11)$$

$$\frac{\rho\partial(Re_{\theta t})}{\partial t}+\frac{\rho\partial\left(V_j Re_{\theta t}\right)}{\partial x_j}=P_{\theta t}+\frac{\partial}{\partial x_j}\left[\sigma_{\theta t}(\mu+\mu_t)\frac{\partial Re_{\theta t}}{\partial x_j}\right]. \qquad (12)$$

This original formulation of the $\gamma-Re_\theta$ features a coupling with the $k-\omega$ SST model, where the production term P_k and the dissipation term D_k of equation 5, and the blending function F_1 of equation 6 are corrected.

3.3.2 Coupling with the SSG-LRR model

The coupling of the SSG-LRR-ω with the $\gamma-Re_\theta$ follows the work developed in [22]. To perform the coupling, the source terms of the turbulent Reynolds stresses equation 9 in the RSM are relaxed using the γ_{eff} variable, in a similar way as with the $k-\omega$ SST model. The production term of the ω equation 10 is also corrected. This results in formulations 13, 14, 15 and 16.

$$\tilde{P_{ij}}=\gamma_{eff}P_{ij}. \qquad (13)$$

$$\tilde{\epsilon_{ij}}=\min(\max(\gamma_{eff},0.1),1.0)\epsilon_{ij}. \qquad (14)$$

$$P_\omega=(1-c_{\mathrm{lam}})P_{SST}+C_{\mathrm{lam}}\,P_{RSM} \qquad (15)$$

$$C_{\mathrm{lam}}=\left\{\begin{array}{ll}0, & c_\omega>\gamma \\ \frac{\gamma-c_\omega}{1-c_\omega}, & c_\omega\le\gamma\end{array}\right. \mathrm{and} c_\omega=\left(\exp\left(-\left(\frac{420}{\tilde{Re}_{\theta t}}\right)^4\right)\right)^2 \qquad (16)$$

Where P_{SST} corresponds to the production term P_w of the ω equation (Eq. 6) for the $k-\omega$ SST model, and P_{RSM} corresponds to the production term P_w of the ω equation (Eq. 10) for the SSG-LRR-ω model.

The final coupling joints the corrected equations 13 to 16 with equation 11 and 12.

3.3.3 Coupling with the $k-\sqrt{k}L$ model

The coupling of the $\gamma-Re_\theta$ transition model with the $k-\sqrt{k}L$ turbulence model is similar to the one used with the $k-\omega$ SST model. This coupling follows the work developed in [25].

4. Non Dimensional Turbulence Quantities

Similarly to k and ω, defined in section 3.1.1, one can define two non-dimensional parameters, the **eddy viscosity ratio** (EVR) and the **turbulence intensity** (Tu), that will represent the turbulent characteristics of the flow.

4.1. Eddy viscosity ratio

The eddy viscosity ratio, EVR, is defined as the ratio between the turbulent viscosity μ_t and the molecular dynamic viscosity of the fluid μ:

$$EVR = \frac{\mu_t}{\mu}. \tag{17}$$

4.2. Turbulence Intensity

The turbulence intensity Tu, is defined as the ratio between the root-mean square of the turbulent velocity fluctuations v, and the mean velocity V:

$$Tu = \frac{v}{V}. \tag{18}$$

We can also define the freestream turbulence intensity (FSTI) as the value of Tu in the freestream.

5. Numerical Solution

5.1. Decay of Turbulence Quantities

The turbulent quantitites will decay along the domain. The evolution of this decay for both the turbulence kinetic energy k and the eddy viscosity μ_t, for the $k-\omega$ SST and the SSG-LRR-ω models is given by equations 19 and 20 [23]:

$$k^* = \frac{k_{in}^*}{\left(1+\beta\left(x^*-x_{in}^*\right)k_{in}^*\left(\frac{\nu}{\nu_t}\right)_{in}Re\right)^{\frac{\beta^*}{\beta}}}, \tag{19}$$

$$\mu_t = \frac{\mu_{tin}}{\left(1+\beta\left(x^*-x_{in}^*\right)k_{in}^*\left(\frac{\nu}{\nu_t}\right)_{in}Re\right)^{\frac{\beta^*}{\beta}-1}}. \tag{20}$$

The subscript $_{in}$ represents the value of the property at the inlet. The superscript * is used to represent non-dimensional quantities. The exception is β^*, that, jointly with β are constants of the equation, available in [3].

It should be mentioned that the decay rate of turbulence is influenced by the chosen freestream values of each one of the properties. The higher the $FSTI$, the more rapid the decay; the lower the μ_t, the more rapid the decay. [33].

When the test-body is located far downstream from the domain inlet, such as in the second and third test-cases - the NLF1-0416 airfoil and the 1:6 prolate spheroid, respectively - the decay is such that the values of this quantity in the body's leading edge reach an assymptotic behaviour. In other words, a change in the inlet value will not imply a change of the value in a point located far downstream of the inlet.

6. Flat Plate Test-Case

This test-case has three main goals:

1. Verify if the result values of C_f converge to a solution when increasing the refinement level of the mesh;
2. Check if transition is affected by the different mesh refinements;
3. Compare the transition characteristics of the RSM with those of the $k-\omega$ SST model, by using turbulent kinetic energy fields;

6.1. Domain

The computational domain used in this study is a rectangle with the incoming flow V_∞ and the plate of length L aligned with the horizontal direction x. The leading edge of the plate is located at the origin of the (x,y) Cartesian coordinate system. The length of the domain is $1.5L$, with the inlet located at $x/L = -0.25$ and the outlet at $x/L = 1.25$. The domain has a height of $0.25L$, being the flat plate located at $y/L = 0$ and the top boundary of the domain at $y/L = 0.25$.

The Reynolds number Re based on the undisturbed freestream velocity V_∞, L, and kinematic viscosity of the fluid ν is 10^7.

6.2. Grids

The grids used were adopted from the AVT 313 workshop [1]. The coarsest grid used is depicted in figure 1, where the different blocks are highlighted with different colours. The grid has a symmetry axis located at the plate's half length ($x/L = 0.5$). This is depicted in image 1:
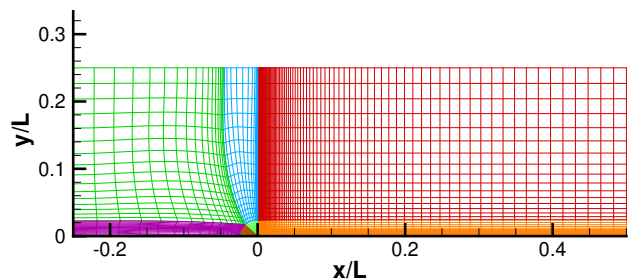

Figure 1: Different blocks that compose the grid used in the flat-plate test-case, highlighted in different colours.

The orthogonal grid starts upstream of the plate's leading edge, in order to ensure a high quality grid at the stagnation region. In the grid refinement studies, different but geometrically similar grids were used. Their characteristics and designation are comprised in table 1:

Table 1: Number of cells in the domain n_c, on the flat plate surface n_s, $((y_n^+)_c)_{max}$ and designation of the several grids used.

	n_c	n_s	$((y_n^+)_c)_{max}$
Grid9	20,840	256	0.92
Grid8	32,000	320	0.76
Grid7	46,080	384	0.66
Grid6	62,720	448	0.58
Grid5	81,920	512	0.52
Grid4	128,000	640	0.44
Grid3	184,320	768	0.38
Grid2	250,880	896	0.33
Grid1	327,680	1024	0.30

7. Numerical Errors

This section intends to illustrate the grid dependance of the RSM and compare it with the one of the $k-\omega$ SST model.

The different inlet turbulence quantities used in this subsection are grouped in six different sets of inlet conditions, which are given in 2:

4

Table 2: Inlet boundary conditions which are kept constant throughout the grid refinement study.

	T3AM		T3A		T3B	
	BC1	BC2	BC1	BC2	BC1	BC2
FSTI	0.01	0.01	0.05	0.05	0.07	0.07
EVR	7.55	0.10	12.67	0.10	99.15	0.10

All these conditions were used in a previous study ([24]). These separate pairs of values aim to represent two different types of transition. **T3AM** corresponds to a case where natural transition occurs. **T3A** and **T3B** correspond to cases where bypass transition occurs.

7.1. Grid Dependance in the RSM and $k - \omega$ SST models

In this subsection, it is possible to verify how the solutions are affected by the grid refinement level, namely:

1. If the values of C_f converge to a solution when increasing grid refinement;
2. If the occurence of transition is affected by the different grid refinements;

This part of the study was performed by plotting the C_f variable against the Re_x variable, for all the case-studies described in table 2.

It was observed that, for all the BC1 conditions (whether for natural or bypass phenomena), there is always the occurrence of transition, independently of the grid refinement level. The latter will only influence the position of the transition: the finer the grid, the further downstream transition occurs. Figures 2 to 3 are given as an example, for the T3AM-BC1 case, both for the RSM and the $k - \omega$ SST model.
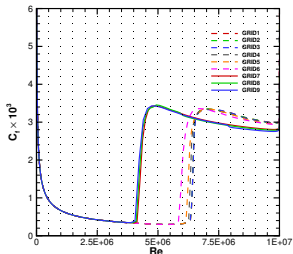
Figure 2: Evolution of the C_f distribution with the grid refinement level for the $T3AM - BC1$ condition for the RSM.
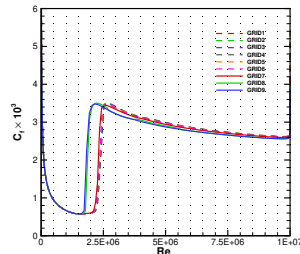
Figure 3: Evolution of the C_f distribution with the grid refinement level for the $T3AM - BC1$ condition for the $k - \omega$ SST.

It is possible to see that when increasing the grid refinement, several phenomena occur. In the T3A and T3AM solutions, where the inlet EVR and FSTI are lower, the results for the RSM present a larger discrepancy between grids than in the T3B solution. Also, the solutions for the finer grids tend to be closer to each other than the ones for the coarser grids. Finally, it can be seen that the solutions for the $k - \omega$ SST model tend to be closer to each other than the ones for the RSM.

Looking at all the BC2 conditions, where the inlet eddy viscosity is considerably smaller (EVR=0.1) than in the BC1 condition, it is possible to see that the RSM only presents transition in the two coarser grids, remaining laminar in the seven finer grids. This behaviour does not occur for the $k - \omega$ SST. This is demonstrated in figures 4 and 5. Only the T3B-BC2 condition

is depicted, but the behaviour obtained for the T3AM-BC2 and T3A-BC2 conditions is similar.
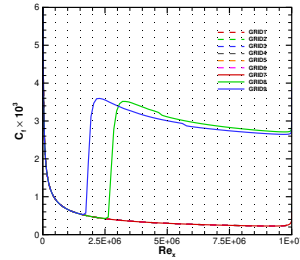
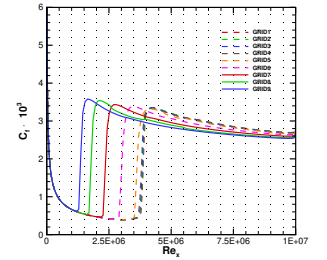Figure 4: Evolution of the C_f distribution with the grid refinement level for the $T3B - BC2$ condition for the RSM.

Figure 5: Evolution of the C_f distribution with the grid refinement level for the $T3B - BC2$ condition for the $k - \omega$ SST.

The results obtained in the finest grid, $grid1$ with the different inlet conditions, for both turbulence models (RSM and $k - \omega$ SST), are compiled in figure 6, which shows that when the inlet EVR is higher (the BC1 cases), the solutions for both models become more similar. In these cases, the C_f curves for the RSM and $k - \omega$ SST present analogous behaviour, but transition happens further downstream for the RSM model.
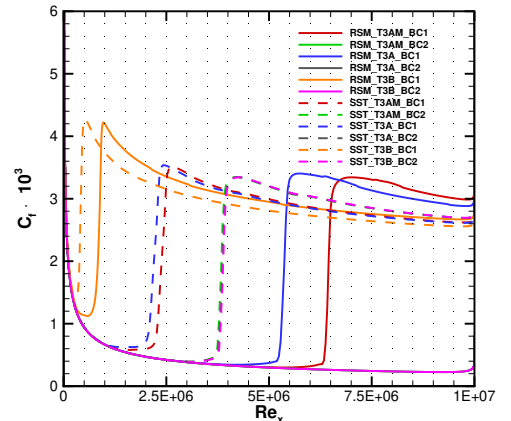
Figure 6: C_f distribution for all the different cases tested with the flat plate, with different inlet turbulence boundary conditions, for the RSM and the $k - \omega$ SST models.

7.2. Influence of Inlet Boundary Conditions - Sensitivity Analysis

In order to try to quantify how much more sensitive to the turbulence inlet conditions the RSM is when compared to the $k - \omega$ SST model, sensitivity studies were carried out. The sensitivity coefficients quantify how much a quantity will vary when another quantity (from which the first one is dependant on) is varied by a fixed amount. In this case, they measure the variation of the x-coordinate (when changing the inlet EVR and the FSTI) for which the C_f is equal to a given value. In each simulation, three different C_f values were used, one corresponding to the beginning of the transition zone, one for the middle, and one for the end. Table 3 feature the sensitivity coefficients calculated for the T3A case, as an example, with the three turbulence models.

Table 3: Sensitivity coefficients to the inlet turbulent boundary conditions calculated for the T3A case, for the beginning, middle, and end of transition, for the three different turbulence models: SSG-LRR-ω, $k - \omega$ SST and $k - \sqrt{k}L$.

	T3A								
	Beginning			**Middle**			**End**		
	$k-\sqrt{k}L$	$k-\omega$ SST	RSM	$k-\sqrt{k}L$	$k-\omega$ SST	RSM	$k-\sqrt{k}L$	$k-\omega$ SST	RSM
FSTI	-0.079	-0.23	-0.32	-0.052	-0.18	-0.20	-0.042	-0.16	-0.19
EVR	-0.67	-0.24	-1.07	-0.54	-0.20	-0.70	-0.50	-0.17	-0.68

7.3. Conclusions

Regarding the numerical errors assessed, several things can be concluded. The RSM presents a greater grid dependence than the $k - \omega$ SST model and needs finer grids than the $k - \omega$ when performing a similar simulation. The difference between the $k-\omega$ SST model and the RSM is augmented when the inlet eddy viscosity is lower, meaning the RSM is especially sensitive to this flow property, which can justify the differences in transition occurence between both models. The RSM model also presents transition downstream of the experimental location, both for natural and bypass transition.

By looking at the sensitivity coefficients obtained, it is possible to draw another broad set of conclusions. All the three turbulence models are more sensitive to changes in the inlet boundary conditions in the T3A case (bypass transition) case, where the base eddy viscosity ratio is higher. Also, the RSM is the most sensitive turbulence model, whether for the FSTI or EVR, in both natural and bypass transition. Besides, the difference between the RSM and the $k - \omega$ SST model is larger in the EVR sensitivity coefficient than in the FSTI. The difference between the RSM and the other models is the largest in the T3A (bypass transition) case, where the base eddy viscosity ratio is higher. In almost all cases, sensitivity coefficients decrease towards the end of the transition, showing the decreasing influence of the inlet conditions along the transition region. The $k - \sqrt{k}L$ model presents the lowest FSTI sensitivity coefficients. However, its EVR sensitivity coefficients are between the ones of the RSM and $k - \omega$ SST model. This suggests that this model presents a different behaviour than the other two, namely when predicting the decay of the inlet turbulence quantities, as explicit in [22].

8. Airfoil Test-Case

The focus of this test-case is on the flow over the NLF1-0416 airfoil. It includes studies regarding the sensitivity to inlet turbulence boundary conditions for both the SSG-LRR ω and the $k - \omega$ SST model, and features a comparison between the SSG-LRR-ω model and the $k - \omega$ SST model regarding their prediction of the location of transition, for similar conditions.

8.1. Domain

The computational domain used in this study is a rectangle with the incoming flow V_∞ and the airfoil's chord c aligned with the horizontal direction x, with a zero angle of attack α. The leading edge of the airfoil is located at the origin of the (x, y) Cartesian coordinate system. The length of the domain in the x direction is $36c$, with the inlet located at $x/c = -12$ and the outlet at $x/c = 24$. The domain has a height in the y direction of $24c$, being the top boundary of the domain located at $y/c = 12$ and the bottom boundary of the domain at $y/c = -12$.

The Reynolds number Re based on the undisturbed freestream velocity V_∞, chord of the airfoil c and kinematic viscosity of the fluid ν is 4×10^6.

8.2. Grids

All the simulations in the airfoil test-case were performed using the same grid, taken from a previous study [25]. Similarly to the ones used in the flat plate test-case, this is comprised by several structured blocks, which feature different levels of refinement according to their location in the domain. The mesh is depicted in figures 7 and 8.
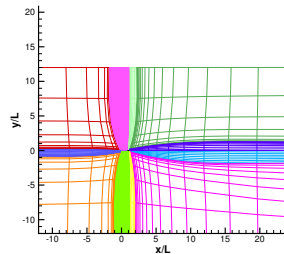

Figure 7: Different blocks that comprise the grid used in the airfoil test-case highlighted in different colours - view of the entire domain.
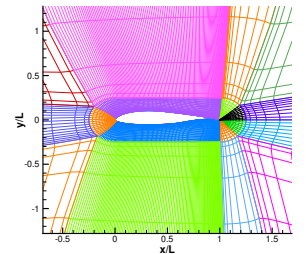
Figure 8: Different blocks that comprise the grid used in the airfoil test-case highlighted in different colours - zoomed view.

8.3. Sensitivity Coefficients

Three different simulations are carried out for each case, summarized in table 5. These allowed to calculate a "minus" and a "plus" coefficient. Besides using the values of these properties at the inlet, two additional sets of sensitivity coefficients were calculated, featuring the $FSTI$ and EVR values in two distinct locations: at a distance of $1c$ from the airfoil's leading edge - $11c$ downstream of the inlet - and at the leading edge itself.

The leading edge of the airfoil is located far downstream - $12c$ - of the inlet, a considerably larger value than what was verified in the flat plate test-case, where the leading edge was located $0.25L$ downstream of the inlet. Therefore, there will be a higher decay of the different turbulent quantities especified at the inlet, with them reaching the assymptotic region described in subsection 5.1 near the leading edge of the airfoil. The results obtained are shown in table 4. Only the coefficients for the upper surface are shown, but the ones for the lower surface follow a similar behaviour.

Table 4: Sensitivity coefficients to the inlet turbulent boundary conditions obtained with the C_f distribution for the upper surface of the NLF1-0416 airfoil using the SSG-LRR-ω and the $k - \omega$ SST models.

			Beginning		Middle		End	
			Minus	Plus	Minus	Plus	Minus	Plus
FSTI	RSM	Inlet	1.260_E-4	8.342_E-5	1.698_E-4	1.051_E-4	2.457_E-4	2.365_E-4
		11x/c	-2.254_E-3	-2.217_E-3	-3.032_E-3	-2.603_E-3	-4.398_E-3	-4.717_E-3
		12x/c	-2.331_E-3	-2.060_E-3	-2.943_E-3	-2.488_E-3	-4.257_E-3	-4.506_E-3
	$k-\omega$ SST	Inlet	-7.200_E-4	8.132_E-5	-4.768_E-4	5.101_E-5	-5.177_E-4	6.465_E-4
		11x/c	-1.285_E-2	-1.211_E-3	-8.505_E-3	-7.638_E-4	-9.224_E-3	-9.432_E-4
		12x/c	-1.243_E-2	-1.197_E-3	-8.627_E-3	-7.431_E-4	-9.362_E-3	-9.545_E-4
EVR	RSM	Inlet	-3.255_E-2	-3.372_E-2	-3.305_E-2	-3.342_E-2	-3.236_E-2	-3.135_E-2
		11x/c	-2.982_E-2	-3.092_E-2	-3.025_E-2	-3.055_E-2	-2.957_E-2	-2.866_E-2
		12x/c	-2.982_E-2	-3.092_E-2	-3.025_E-2	-3.055_E-2	-2.957_E-2	-2.866_E-2
	$k-\omega$ SST	Inlet	-6.645_E-2	-5.982_E-2	-5.572_E-2	-5.322_E-2	-6.522_E-2	-5.945_E-2
		11x/c	-6.090_E-2	-5.598_E-2	-5.169_E-2	-4.883_E-2	-5.977_E-2	-5.443_E-2
		12x/c	-6.090_E-2	-5.598_E-2	-5.169_E-2	-4.883_E-2	-5.977_E-2	-5.443_E-2

Upper Surface

Figure 9: C_f curves obtained for the five different sets of turbulent inlet conditions, both for the SSG-LRR-ω and the $k - \omega$ SST. The filled lines represent the reults obtained for the SSG-LRR-ω model and the dashed lines for the $k - \omega$ SST model. Green lines correspond to the results for the upper surface, and blue lines for the lower surface.

Table 5: Inlet turbulence boundary conditions used for the determination of the sensitivity coefficients to the inlet EVR and FSTI for the airfoil test-case.

EVR			
EVR($\frac{\mu_t}{\mu}$)	45	50	55
FSTI	0.03	0.03	0.03

FSTI			
EVR($\frac{\mu_t}{\mu}$)	50	50	50
FSTI	0.02	0.03	0.04

The overall coefficients calculated at the inlet are considerably small, and therefore should not be accepted as significant, since they do not fairly represent the variations of the inlet turbulence boundary conditions in regions close to the airfoil. Both the FSTI and EVR inlet coefficients are larger for the $k-\omega$ SST model than for the RSM, but within the same order of magnitude. For both models, the inlet coefficients are much smaller for the FSTI than for the EVR, with the difference being of two orders of magnitude. For the FSTI, in both models is verified a decrease of one order of magnitude of the value of the coefficients between the inlet and the regions near/at the leading edge of the airfoil. For the EVR, the values remain fairly constant along the three locations.

8.4. Comparison between the $k-\omega$ SST and the SSG-LRR-ω

The results obtained for all the cases described in table 5, used to calculate the sensitivity coefficients in subsection 8.3, were extremely similar. The curves of C_f for the upper and lower surfaces of the airfoil, both for the RSM and the $k - \omega$ are depicted in figure 9:
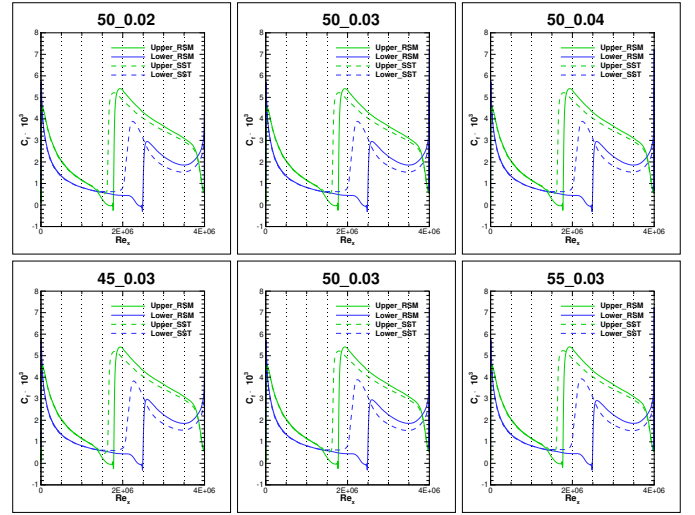
Analysing the results, several aspects can be noticed. The $k-\omega$ SST predicts transition upstream of the SSG-LRR-ω, both for the upper and lower surface. The SSG-LRR-ω presents a region with negative C_f values just before the start of transition. This implies that, in the RSM, the adverse pressure gradient makes the laminar boundary layer separate before the transition to turbulent regime. This does not happen in the $k - \omega$ SST. In this laminar regime, the C_f value predicted by both models is similar. However, after transition occurs, the SSG-LRR-ω predicts a slightly higher value of C_f. This may arise from the ability to deal with turbulence anisotropy of this model, predicting turbulence more accurately along the curve surface of the airfoil in turbulent regime. It can be seen that the difference between both models in the prediction of transition position is smaller in the upper surface, where the pressure gradient is more adverse, when compared to the lower surface.

9. Spheroid Test-Case

This final test-case presents the analysis of the flow over a 6:1 spheroid at an angle of attack of $5°$. The goal of this chapter is to evaluate how the RSM behaves in predicting transition over the surface of the spheroid, and compare it with the results obtained for the $k - \omega$ SST model. It is eventually shown that the inlet conditions tuned for being used with the $k - \omega$ SST may not be the most suitable to be used with the SSG-LRR-ω, even though the transition model coupled with both these models is the same.

9.1. Domain

The 6:1 prolate spheroid with length L is embedded in a three dimensional computational domain, shaped like a rectangular prism, with a length of $200L$ a height of $200L$ and a width of $100L$. The incoming flow V_∞ is alligned with the horizontal direction x. The major axis of the spheroid is parallel to the xy plane, and is oriented in an angle of attack α of $5°$ with the x direction. The center of the spheroid is located at the origin of the (x, y, z) Cartesian coordinate system. The inlet is located at $x/L = -100$ and the outlet at $x/L = 100$. The domain has a lateral boundary located at $z/L = 100$ and a

symmetry boundary condition at $z/L = 0$. The top boundary of the domain is placed at $y/L = 100$ and the bottom boundary of the domain at $y/L = -100$.

The Reynolds number Re based on the undisturbed freestream velocity V_∞, length of the spheroid L and kinematic viscosity of the fluid ν is 6.5×10^6.

9.2. Grids

The simulations of the spheroid test-case were performed using always the same grid, which is comprised by several structured blocks. Figures 10 and 11 intend to represent different parts of this grid that are worth noticing.
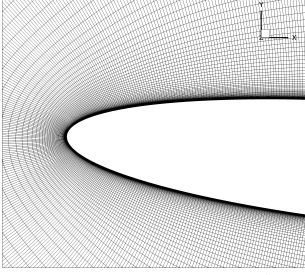
Figure 10: Detailed view of the grid zoomed near the leading edge of the spheroid. The grid is considerably more refined in the regions adjacent to the body, to better capture the near-wall phenomena.
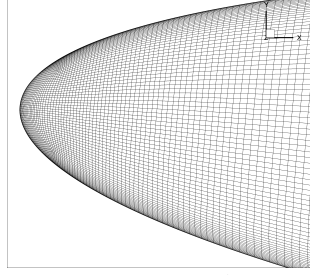
Figure 11: Depiction of the grid used on the spheroid's surface, near its leading edge. This grid structure is symmetric in relation to the spheroid's mid planes, and so the region near the trailing edge will present an identical configuration.

9.3. Results

The values used in the initial simulation - Case1 - provide a value of 0.15% of Tu in the leading edge of the spheroid, to match the values proposed by [11], for a simulation with the 6:1 prolate spheroid test-case with the $k-\omega$ SST model. This simulation did not converge, and presented a large region of laminar separation. On the other hand, for the same inlet turbulence boundary conditions, the $k-\omega$ SST model, without crossflow transition prediction, presented transition to turbulent regime, and a considerably smaller separation bubble upstream of it. This can be observed in figures 12 and 13. Upon this conclusion, several cases were run, trying to evaluate how the turbulence inlet conditions affected the solution. These cases are presented in table 6. The reasoning behind the chosen values for each simulation ought to be explained:

- Case2 was run with same conditions as Case1, but with no transition model, to perceive if the difference in the transition prediction between Case1 and the results obtained for the $k-\omega$ SST were related to the coupling with the $\gamma - Re_\theta$ transition model;
- Since Case2 did converge, the inlet turbulence quantities were increased, to the values of Case3, and the transition model was again coupled with the SSG-LRR-ω. Cases 3 to 6 were run in order to find a lower limit of the turbulence quantities in the LE of the spheroid for which the SSG-LRR-$\omega + \gamma - Re_\theta$ did not converge anymore, which was achieved in Case6. Due to the increased inlet turbulence quantitites, these simulations did not present laminar separation bubble, as in Case1. This can be seen in figure 14;

- Case7 had the goal of mimicking the turbulence intensity at the leading edge of Case6, but with a much higher value of EVR and lower value of FSTI at the inlet, to verify if the iterative convergence was achieved for the same conditions at the LE but with a higher EVR at the inlet;
- Finally Case8 was run to perceive if iterative convergence was achieved with the lower value of FSTI at the LE with which the simulation had converged - Case5, but with a higher value of inlet FSTI, and the lowest possible value of EVR at the inlet [25].

Table 6: Description of all the cases used to study the flow over the 6:1 spheroid, regarding the usage of transition model, the turbulence quantities in several points, flow separation, and iterative convergence. "T.M." stands for transition model, "Sep." stands for "flow separation" and "Conv." stands for convergence

| Case	T.M	Inlet EVR	Inlet FSTI (%)	LE EVR	LE FSTI (%)	TE EVR	TE FSTI (%)	Sep.	Conv.
1	Yes	250	0.500	206.455	0.151	206.295	0.150	Yes	No
2	No	250	0.500	206.455	0.151	206.295	0.150	No	Yes
3	Yes	8000	5.000	6024.222	0.849	6019.186	0.845	No	Yes
4	Yes	8000	0.580	7800.101	0.495	7798.382	0.494	No	Yes
5	Yes	800	0.580	703.606	0.260	703.133	0.259	No	Yes
6	Yes	800	0.350	746.110	0.226	745.751	0.226	-	No
7	Yes	2000	0.257	1959.496	0.226	1959.137	0.226	-	No
8	Yes	800	2.780	547.357	0.259	546.888	0.258	No	Yes
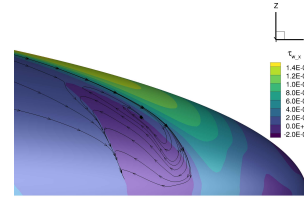
Figure 12: Map of the skin-friction in the x direction on the surface of the spheroid using the SSG-LRR ω model with 0.15 % of FSTI at the LE of the spheroid. The streamlines show the recirculation of the flow inside the large separation bubble that is formed.
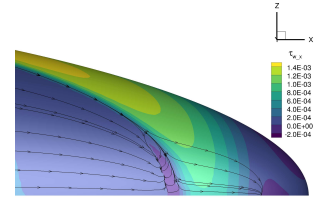

Figure 13: Map of the skin-friction in the x direction on the surface of the spheroid using the $k-\omega$ SST model with 0.15 % of FSTI at the LE of the spheroid. The recirculation of the flow shown by the streamlines highlights a much smaller separation bubble than in the RSM.
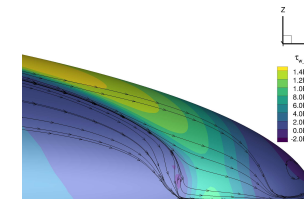

Figure 14: Map of the skin-friction in the x direction on the surface of the spheroid using the SSG-LRR-ω with Case4. The streamlines show that there is no recirculation of the flow as in Case1.
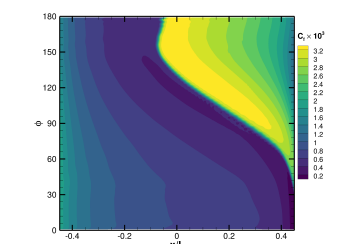

Figure 15: C_f distribution on the unrolled surface of the prolate spheroid obtained for Case1 with the $k-\omega$ SST model.

Figures 16 to 21 show the C_f distributions obtained with the SSG-LRR-ω for all the converged cases mentioned in table 6,

as well as Case1. Figure 15 shows the C_f distribution obtained with the $k-\omega$ SST model, for Case1. In these figures, the y axis represents the azimuthal angle ϕ of a given point at the surface of the spheroid [19], and the x axis represents the spheroid's non-dimensional length x/L. Except for figure 16, whose solution did not converge, the C_f distributions are in line with the expected results:

1. Figure 15 displays the results obtained for Case1 with the $k-\omega$ SST model, and show transition occurring fairly downstream of the location predicted by the SSG-LRR-ω for the same case, but with no transition model, patent in figure 17;

2. Figure 17 presents Case2, with no transition model coupled with the SSG-LRR-ω. The high values of C_f on the left side of the map mean that transition occurs fairly close of the leading edge, considerably upstream of what occurs in all other cases that feature the coupling of the SSG-LRR-ω with the $\gamma - Re_\theta$ model;

3. From Case3 to Case5, in figures 18 to 19, transition occurs further downstream in each case, due to the successive decrease of the inlet turbulence quantitites. This is understandable, since larger values of inlet FSTI and EVR will prompt transition to occur earlier;

4. Case8, presented in figure 21 is comparable to Case5, in figure 19, since they both present the same value of 0.26% for the turbulence intensity at the leading edge of the spheroid. However, the higher value of FSTI at the inlet in Case8 causes transition to be triggered earlier than in Case5.
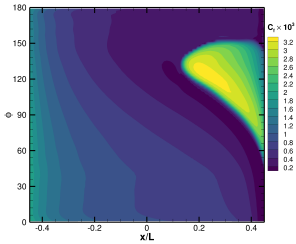

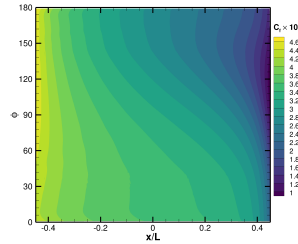Figure 16: C_f distribution on the unrolled surface of the prolate spheroid obtained for Case1, with the SSG-LRR-ω model.

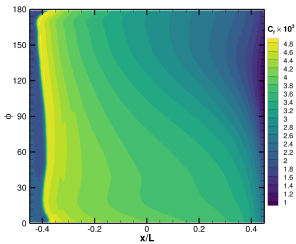Figure 17: C_f distribution on the unrolled surface of the prolate spheroid obtained for Case2, with the SSG-LRR-ω model.

Figure 18: C_f distribution on the unrolled surface of the prolate spheroid obtained for Case3, with the SSG-LRR-ω model.
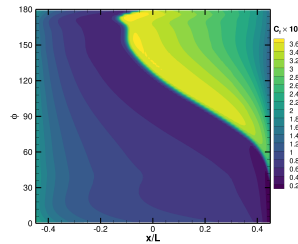

Figure 19: C_f distribution on the unrolled surface of the prolate spheroid obtained for Case4, with the SSG-LRR-ω model.

Looking at figures 16 to 21, several conclusions may be withdrawn:

1. The inlet turbulence boundary conditions tuned for being used with the $k-\omega$ SST model are not suitable for being used with the SSG-LRR-ω model with this latter needing a greater turbulence intensity to display the same results
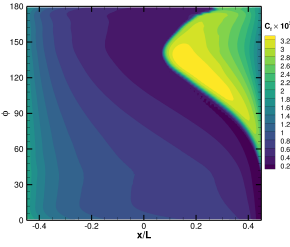

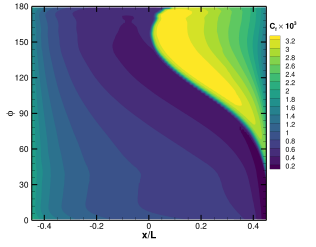Figure 20: C_f distribution on the unrolled surface of the prolate spheroid obtained for Case5, with the SSG-LRR-ω model.

Figure 21: C_f distribution on the unrolled surface of the prolate spheroid obtained for Case8, with the SSG-LRR-ω model.

of the $k-\omega$ SST model;

2. For identical inlet turbulence boundary conditions, especially for relatively low values, the RSM tends to present larger regions with flow separation, with its inherent recirculation, than the $k-\omega$ SST. This occurs because the RSM delays the occurence of transition and then inherently what happens is laminar separation.

3. The $k-\omega$ SST model can converge to a result in situations where the RSM can present some iterative convergence difficulties, namely in regions of instability, such as the large separation bubble yielded in Case1.

10. Conclusions

This final section intends to summarize the achievements and conclusions obtained in the different test-cases, whilst providing some ideas for future work developed in this area.

10.1. Numerical Robustness of the SSG-LRR-$\omega + \gamma - Re_\theta$ coupling

Along almost all the simulations performed in this work, the SSG-LRR-ω model demonstrated to have a satisfactory iterative convergence, with no major problems in reducing the residuals to negligible levels. However, in general, it proved to have more difficulties in converging to a solution than the $k-\omega$ SST model, i.e., it took a larger number of iterations. Additionally, in some situations of large regions of instability, such as separation bubbles, the RSM could not converge to a solution, whilst the $k-\omega$ SST model could. The RSM presented a greater grid dependence, and needed a finer grid than the $k-\omega$ SST model to present similar results. The uncertainty of the calculation of transition position when increasing the grid refinement is larger in the RSM than in the $k-\omega$ SST.

10.2. Transition Prediction

In this work was concluded that the SSG-LRR-ω tends to present transition downstream of the location predicted by the $k-\omega$ SST model. In some specific cases, when the values of the inlet turbulence boundary conditions are lower, the RSM may not be able to match the experimental data and the values predicted by the $k-\omega$ SST: these latter two exhibit transition whilst the RSM predicts a full laminar solution.

10.3. Influence of the decay of the turbulence inlet conditions

The decay of the FSTI is more accentuated than the one of the EVR, meaning that variations of the inlet value of the EVR will have a greater impact on the simulation results than variations of the inlet FSTI - greater decay of the FSTI will imply

that a variation on the inlet is not translated into a variation near a test-body located far downstream from the inlet. The higher the value of the inlet turbulence boundary conditions, the greater the sensitivity of the models studied to changes in these conditions. From all the models studied, the SSG-LRR-ω appeared to be the most sensitive. It was also found out that the inlet turbulence boundary conditions tuned to be used with the $k - \omega$ SST are not the most suitable to be used with the SSG-LRR-ω.

10.4. Future Work

With the conclusions withdrawn from the work developed, it is possible to define some future work to be carried out regarding this topic. It would be interesting to study a method to obtain the appropriate inlet turbulence boundary conditions to be used in a study with the SSG-LRR-ω, taking the conditions tuned for the $k - \omega$ SST as a starting point, since this latter is a more commonly used model, and therefore there is plenty of accessible data for it. The experimental data available could also be used to tune these conditions for the RSM. Another suggestion would be to include the crossflow prediction method in this coupling, and assess if the differences observed in the spheroid test-case between the $k - \omega$ SST and the SSG-LRR-ω would persist. The crossflow prediction would also be useful to better compare the results obtained in this test-case with the experimental ones. Stability studies could be carried out, in order to perceive if would be worth to develop additional tools to ensure the iterative convergence of the SSG-LRR-ω in a broad set of conditions, i.e, when there are large instability regions, or if the test-body presents a complex geometry. Finally, it would be fruitful to compare the performance of the SSG-LRR-ω with other turbulence models in environments that theoretically suit this model the most [17]. To seize all the advantages coming from the ability to deal with the turbulence anisotropy, some test-cases could be studied, such as delta wings, oblate spheroids, or even moving cylinders.

References

[1] Avt 313 workshop. http://web.tecnico.ulisboa.pt/ist12278/Workshop_AVT_313_2D_cases/Workshop_AVT_313_2D_cases.htm. Accessed: 2020-10-30.

[2] Langtry-menter 4-equation transitional sst model. https://turbmodels.larc.nasa.gov/langtrymenter_4eqn.html. Accessed: 2020-09-30.

[3] Menter shear stress transport turbulence model. https://turbmodels.larc.nasa.gov/sst.html. Accessed: 2020-09-30.

[4] Refresco software features. https://www.marin.nl/facilities-and-tools/software/refresco. Accessed: 2021-02-15.

[5] Ssg/lrr full reynolds stress model. https://turbmodels.larc.nasa.gov/rsm-ssglrr.html. Accessed: 2020-09-30.

[6] K. Bhaganagar, D. Rempfer, and J. Lumley. Direct numerical simulation of spatial transition to turbulence using fourth-order vertical velocity second-order vertical vorticity formulation. *Journal of Computational Physics*, 180(1):200–228, 2002.

[7] J. Boussinesq. *Théorie analytique de la chaleur mise en harmonic avec la thermodynamique et avec la théorie mécanique de la lumière: Tome I-II*, volume 2. Gauthier-Villars, 1903.

[8] C. Cambon, L. Jacquin, and J. Lubrano. Toward a new reynolds stress model for rotating turbulent flows. *Physics of Fluids A: Fluid Dynamics*, 4(4):812–824, 1992.

[9] R. Cécora, R. Radespiel, B. Eisfeld, and A. Probst. Differential reynolds-stress modeling for aeronautics. *AIAA Journal*, 53(3):739–755, 2015.

[10] R. Cécora, R. Radespiel, B. Eisfeld, A. Probst, S. Crippa, and R. Radespiel. Differential reynolds stress modeling for aeronautics. In *50th AIAA Aerospace Sciences Meeting including the New Horizons forum and aerospace exposition*, page 465, 2012.

[11] J. Coder. Standard test cases for transition model verification and validation in computational fluid dynamics. In *2018 AIAA Aerospace Sciences Meeting*, pages 2018–0029, 2018.

[12] A. Dewan. Reynolds-averaged governing equations and closure problem. In *Tackling Turbulent Flows in Engineering*, pages 43–48. Springer, 2011.

[13] D. Di Pasquale, A. Rona, and S. Garrett. A selective review of transition modelling for cfd. In *39th AIAA fluid dynamics conference*, page 3812, 2009.

[14] P. Durbin. Turbulence closure models for computational fluid dynamics. *Encyclopedia of Computational Mechanics*, 3, 2004.

[15] B. Eisfeld and O. Brodersen. Advanced turbulence modelling and stress analysis for the dlr-f6 configuration. In *23rd AIAA Applied Aerodynamics Conference*, page 4727, 2005.

[16] B. Eisfeld, C. Rumsey, and V. Togiti. Verification and validation of a second-moment-closure model. *AIAA Journal*, 54(5):1524–1541, 2016.

[17] Y. Hassan. An overview of computational fluid dynamics and nuclear applications. *Thermal-Hydraulics of Water Cooled Nuclear Reactors*, pages 729–829, 2017.

[18] S. Keye and O. Brodersen. Investigations of fluid-structure coupling and turbulence model effects on the dlr results of the fifth aiaa cfd drag prediction workshop. In *31st AIAA Applied Aerodynamics Conference*, page 2509, 2013.

[19] G. Korn and T. Korn. Mathematical handbook for scientists and engineers. *New York*, 1968.

[20] R. Langtry and F. Menter. Correlation-based transition modeling for unstructured parallelized computational fluid dynamics codes. *AIAA Journal*, 47(12):2894–2906, 2009.

[21] B. Launder, G. J. Reece, and W. Rodi. Progress in the development of a reynolds-stress turbulence closure. *Journal of fluid mechanics*, 68(3):537–566, 1975.

[22] R. Lopes. *Simulation of Transition from Laminar to Turbulent Regime in Practical Applications of Incompressible Flow*. PhD thesis, IST, 2021.

[23] R. Lopes, L. Eça, and G. Vaz. On the decay of free-stream turbulence predicted by two-equation eddy-viscosity models. In *20th Numerical Towing Tank Symposium*, pages 133–138, 2017.

[24] R. Lopes, L. Eça, and G. Vaz. On the numerical behavior of rans-based transition models. *Journal of Fluids Engineering*, 142(5), 2020.

[25] R. Lopes, E. Fernandes, L. Eça, G. Vaz, and M. Kerkvliet. Coupling two correlation-based transition models to the k- k l eddy viscosity turbulence model. *AIAA Journal*, 59(5):1735–1748, 2021.

[26] F. Menter. Improved two-equation k-omega turbulence models for aerodynamic flows. *Nasa Sti/recon Technical Report N*, 93:22809, 1992.

[27] F. Menter, Y. Egorov, and D. Rusch. Steady and unsteady flow modelling using the kskl model. In *Turbulence Heat and Mass Transfer 5. Proceedings of the International Symposium on Turbulence Heat and Mass Transfer*. Begel House Inc., 2006.

[28] F. Menter, R. Langtry, S. Likki, Y. Suzen, P. Huang, and S. Völker. A correlation-based transition model using local variables—part i: model formulation. 2006.

[29] F. R. Menter, P. E. Smirnov, T. Liu, and R. Avancha. A one-equation local correlation-based transition model. *Flow, Turbulence and Combustion*, 95(4):583–619, 2015.

[30] S. Nie. *Extension of transition modeling by a transport equation approach*. PhD thesis, DLR, 2017.

[31] T. Sayadi, C. Hamman, and P. Moin. Direct numerical simulation of complete h-type and k-type transitions with implications for the dynamics of turbulent boundary layers. *Journal of Fluid Mechanics*, 724:480, 2013.

[32] T. Sayadi and P. Moin. Large eddy simulation of controlled transition to turbulence. *Physics of Fluids*, 24(11):114103, 2012.

[33] P. Spalart and C. Rumsey. Effective inflow conditions for turbulence models in aerodynamic calculations. *AIAA Journal*, 45(10):2544–2553, 2007.

[34] C. Speziale, S. Sarkar, and T. Gatski. Modelling the pressure–strain correlation of turbulence: an invariant dynamical systems approach. *Journal of fluid mechanics*, 227:245–272, 1991.

[35] J. Van Ingen. The en method for transition prediction. historical review of work at tu delft. In *38th Fluid Dynamics Conference and Exhibit*, page 3830, 2008.